Towards a mechanistic understanding of the sol-gel syntheses of ternary carbides

Journal:	*Inorganic Chemistry Frontiers*
Manuscript ID	QI-RES-01-2022-000053.R2
Article Type:	Research Article
Date Submitted by the Author:	14-Feb-2022
Complete List of Authors:	Siebert, Jan Paul ; Arizona State University, School of Molecular Sciences Juelsholt, Mikkel; University of Copenhagen, Nano-Science Center & Department of Chemistry Günzing, Damian; Universität Duisburg-Essen Wende, Heiko; Universität Duisburg-Essen, Faculty of Physics Ollefs, Katharina; Universität Duisburg-Essen, Faculty of Physics and Center for Nanointegration Duisburg-Essen (CENIDE) Birkel, Christina; Technische Universitat Darmstadt, Eduard-Zintl-Insitut für Anorganische Chemie

SCHOLARONE™
Manuscripts

ARTICLE

Towards a mechanistic understanding of the sol-gel syntheses of ternary carbides

Jan P. Siebert[a], Mikkel Juelsholt[b], Damian Günzing[c], Heiko Wende[c], Katharina Ollefs[c], Christina S. Birkel*[a,d]

Sol-gel chemistry, while being extremely established, is to this day not fully understood, and much of the underlaying chemistry and mechanisms are yet to be unraveled. Here, we elaborate on the sol-gel chemistry of Cr_2GaC, the first layered ternary carbide belonging to the MAX phase family to ever be synthesized using this wet chemical approach. Leveraging a variety of both in- and ex-situ characterization techniques, including X-ray and neutron powder diffracion, X-ray absorption fine structure analyses, total scattering analyses, and differential scanning calorimetry coupled with mass spectrometry, in-depth analyses of the local structures and reaction pathways are elucidated. While the metals first form tetrahedrally and octahedrally coordinated oxidic structures, that subsequently grow and crystallize into oxides, the carbon source citric acid sits on a separate reaction pathway, that does not merge with the metals until the very end. In fact, after decomposing it remains nanostructured and disordered graphite until the temperature allows for the reduction of the metal oxides into the layered carbide. Based on this, we hypothesize that the method is mostly applicable to systems where the needed metals are reducebale by graphite around the formation temperature of the target phase.

Introduction

Sol-gel chemistry is among the very traditional and established techniques in chemistry, and dates back to as early as 1846[1] when Ebelmen discovered the spontaneous gel-formation of a $SiCl_4$-derived alkoxide. Now, more than 150 years later, the underlaying processes – hydrolysis and condensation – have been widely studied and applied to a plethora of systems. Initially developed for the synthesis of oxides,[2] carbides,[3,4] nitrides,[5] and borides[6] are nowadays also accessible through sol-gel chemistry.[7] Furthermore, the number of possible sol-gel starting materials knows almost no limit and has been vastly diversified from the original alkoxide-based chemistry and includes, for instance, small molecule routes as well as polymer-based gels. As a result, the obtainable range of materials, compositions, morphologies, and microstructures is enormous.[7] For instance, besides oxides in complex quaternary stoichiometries,[2] non-oxidic (hollow) microspheres[8] and thick films,[8] as well as microwires[9] have been successfully synthesized.

However, in contrast to its long history and amount of research that has been dedicated to sol-gel chemistry, the reaction mechanisms still need to be fully understood today. While the community has agreed on basic processes involved in the gel-forming and combustion step – i.e. hydrolysis and condensation reactions followed by solid-to-solid crystallizations[10] – these concepts are still rather broadly described.[7] Furthermore, an overwhelming majority of studies focus on oxidic systems,[10] in part due to the simplified experimental setup, that does not require controlled atmospheres. For a controlled synthesis targeting specific properties and compositions understanding the mechanism is essential.[11] Particularly in the lesser studied carbide and nitride systems this has proven to be critical. Schnepp et al.,[12] for instance, demonstrated the need for such in-depth studies for the Fe_3N/Fe_3C system in elucidating the reaction pathway. Here, the nitride phase was shown to be the intermediate product, emphasizing how important the understanding of reaction mechanisms is when specific (metastable) products are targeted. In a different work, the sol-gel controlled synthesis of YBCO ($YBa_2Cu_4O_8$) nanowires[13] was found to be enabled via the restricted nucleation in the gel-matrix. The investigation into the mechanism revealed that the hindered nucleation of $BaCO_3$ crystals allows them to act as tiny catalysts from which the nanowires start to grow. Additionally, that specific behavior has a direct impact on the nanowires' superconductivity, as this property depends on the local microstructure. A more exotic example by Charpentier et al.[14] beautifully demonstrates another facet to mechanistic studies: the discovery of entirely new reaction pathways. Their work in supercritical CO_2 revealed a substitution-condensation process, as opposed to the generally accepted hydrolysis and condensation route.

With high performing materials in increasing demand, this in-depth insight is directly needed to rationally design syntheses, particularly for more complex systems and technologically useful morphologies. In the case of ternary carbides and nitrides, MAX phases have attracted considerable interest during the past 25 years. This family of compounds ($M_{n+1}AX_n$) crystallizes in a hexagonal crystal structure ($P6_3mmc$). Hereby, M are mainly early transition metals, A represents main group (semi)metals, and X is either carbon or nitrogen. Originally discovered by Kudielka and Rohde[15] in 1960, and classified by Nowotny and coworkers[16] shortly after, they've been of great scientific interest ever since the works of Barsoum and coworkers.[17]

[a.] School of Molecular Sciences, Arizona State University, Tempe AZ-85282, USA. Email: Christina.Birkel@asu.edu
[b.] Department of Chemistry, University of Copenhagen, 2100 Copenhagen, DEN.
[c.] Faculty of Physics and Center for Nanointegration Duisburg-Essen (CENIDE), University of Duisburg-Essen, Lotharstraße 1, 47057 Duisburg, Germany
[d.] Department of Chemistry and Biochemistry, Technische Universität Darmstadt, Germany

In fact, they can be described as metallic ceramics or ceramic metals due to the unusual combination of both metallic and ceramic properties, including electrical conductivity, stiffness, chemical resistance, and damage tolerance to name a few.[18] These properties originate in the layered crystal structure of MAX phases. The edge-sharing M_6X octahedra form a layer, that expands only on a 2D plane (for n = 1). Higher order MAX phases (n > 1) add additional MX layer to the structure, however, the octahedra "multilayer" still primarily extends in a 2D plane. The A element sits as a single layer in between the octahedra, and is coordinated by the M element in a trigonal prismatic fashion. Figure 1 depicts the (extended) crystal structure, showing the octahedra layers interleaved by the atomic layer of A.

It has previously been demonstrated[4,19] that sol-gel chemistry is a viable, versatile, and new technique in the MAX phase community, however, the reaction pathway has not been fully elucidated. This study therefore aims to improve the mechanistic understanding of the sol-gel synthesis of Cr_2GaC. For this purpose, neutron powder diffraction (NPD), X-ray diffraction (XRD), neutron and X-ray total scattering with pair distribution function analysis (PDF), *ex-situ* X-ray absorption spectroscopy (EXAFS), *in-situ* differential scanning calorimetry in conjunction with mass spectrometry (DTA-MS), and electron microscopy (SEM, EDS) analyses were carried out. Based on the initial results reported for Cr_2GaC,[4] the mechanism is significantly refined and expanded on.

Experimental

The sol-gel synthesis of Cr_2GaC for *ex-situ* studies is described in detail elsewhere.[4] In short, the metal nitrates and citric acid (Ga-nitrate and citric acid obtained from Alfa Aesar, Cr-nitrate purchased from Sigma Aldrich, all used without further manipulation), where dissolved in deionized water in a 2:1:9 ratio according to the MAX phase stoichiometry, whereby citric acid was used in a ninefold excess. Calcinating the resulting gel at 1050 °C for 5 hours under flowing Ar yields the MAX phase. A detailed synthesis protocol can be found in the SI.

For various *ex-situ* investigations (NPD, synchrotron XRD, PDF, EXAFS), the reaction was terminated at specific temperatures (early to mid-stage between 300 °C and 600 °C; around the crystallization temperature of 700 °C; and the late to final stage at 800 °C and 1050 °C) to gain insights into the reaction pathway. In case of *in-situ* experiments (DTA-MS), the gel was prepared as described and fully dried at 100 °C overnight prior to the measurement. Synchrotron XRD and total scattering data were collected at Deutsches Elektronen Synchrotron (DESY) at beamline P02.1. The samples were loaded into a 1 mm Kapton capillary and measured with a wavelength of λ = 0.207 Å. To obtain the PDFs, the X-ray scattering signal from an empty Kapton tube was used for background subtraction. The X-ray PDFs were obtained using PDFgetX3[20] in XPDFsuite.[21] Neutron total scattering experiments were carried out at Oakridge National Laboratory's Spallation Neutron Source using the Nanoscale-Ordered MAterials Diffractometer (NOMAD).[22] Here, the samples were loaded in 3 mm diameter quartz capillaries, which were measured against an empty reference capillary to reduce background noise. Using the in-house program ADDIE[23] the obtained data were reduced. The neutron PDF was obtained via PDFgetN3[24] out of the $S(Q)$ extracted with ADDIE. Total scattering data were refined using PDFgui[25] and more information on the PDF modelling can be found in the Supporting Information.

EXAFS experiments were carried out at Diamond Light Source using beam line B18 for the Cr K-edges and the Ga K-edges. Data were collected in transmission mode at ambient temperatures. Further data analysis was carried out with the software packages FEFF and Larch, which utilizes the fitting tool FEFFIT.[26,27]

Electron microscopy was carried out on carbon tape, whereby a Zeiss Auriga microscope equipped with an energy dispersive spectroscopy (EDS) silicon drift detector (SDD) (Oxford Instruments, Ultim MAX) was used, with accelerating voltages ranging from 5 to 20 keV. To prepare samples, the ground powder was attached to the sample holder using carbon tape. Calorimetry measurements were carried out on a Netzsch STA 449 F3 Jupiter® (DTA) with an on-line mass spectrometer (WMS 403 Aelos) under flowing Ar. The reader is again referred to the SI for full details.

Results and discussion

Before discussing the mechanistic details of this study, the results of the synthesis and characterization of Cr_2GaC are laid out. Figure 1 presents the structural characterization of Cr_2GaC, as obtained from the sol-gel synthesis. The refined XRD data reveal mainly the target MAX phase, however, a side phase can be identified. With about 16 wt-%, Cr_3C_2 accounts for a smaller fraction in the final product. This impurity is not surprising, as it represents a stable binary compound. Considering the large amounts of carbon available in the system (see Figure 1 (d) EDS data), the formation of a carbon-rich phase is to be expected. In the present system, only Cr is known to form binary carbides, explaining the observed phase composition. The refined unit cell parameters a = 2.89129(3) Å and
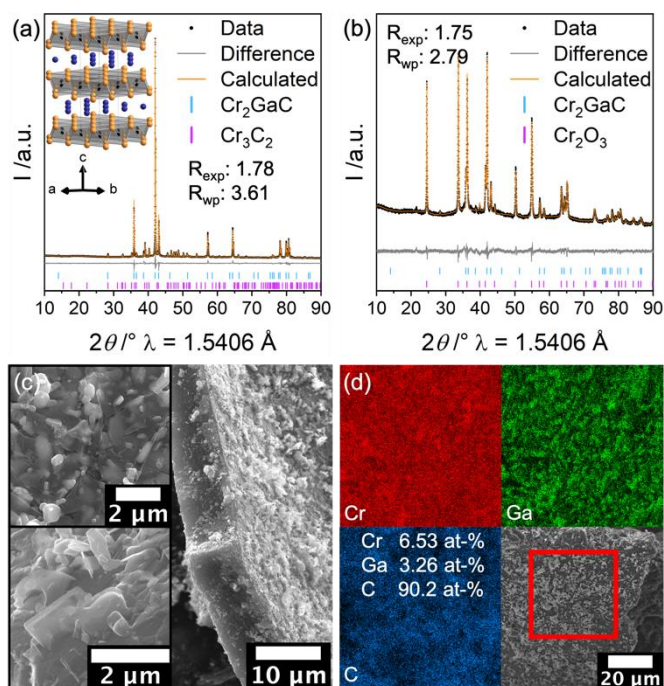

Figure 1: (a) and (b) Rietveld refinement of XRD data of Cr_2GaC synthesized at 1050 °C and 800 °C, respectively. Data shown in black (dots), refinement shown in orange, and the difference curve is shown in grey. The refined phases are indicated by their respective *hkl* markers.[28,42,43] **(c)** SEM micrographs showing the particle morphology at different magnifications. **(d)** SEM EDS showing the homogeneous distribution as well as the 2:1 ratio of Cr and Ga.

c = 12.6090(2) Å match the originally reported values well.[28] Full refinement details can be found in Tables S 1 – S 4 (SI). As expected,

based on the previously reported work,[4] lower reaction temperatures (800 °C, Figure 1(b)) result primarily in the formation of oxides (see also SI for more refinement details). The microstructural analysis of Cr_2GaC is also shown in Figure 1 (c) and reflects the typical busy morphology shown elsewhere.[4] The layered nature of the MAX phase is clearly visible at higher magnifications, whereby the layers themselves are randomly oriented, stemming from the uncontrolled crystal growth during the combustion step. The elemental analysis shown in Figure 1 (d) demonstrates the homogenous distribution of all elements, while no other impurities can be detected. The excess carbon is also noticeable in the quantification, which is a result of the citric acid excess needed to achieve a full reaction conversion (see mechanistic study below).
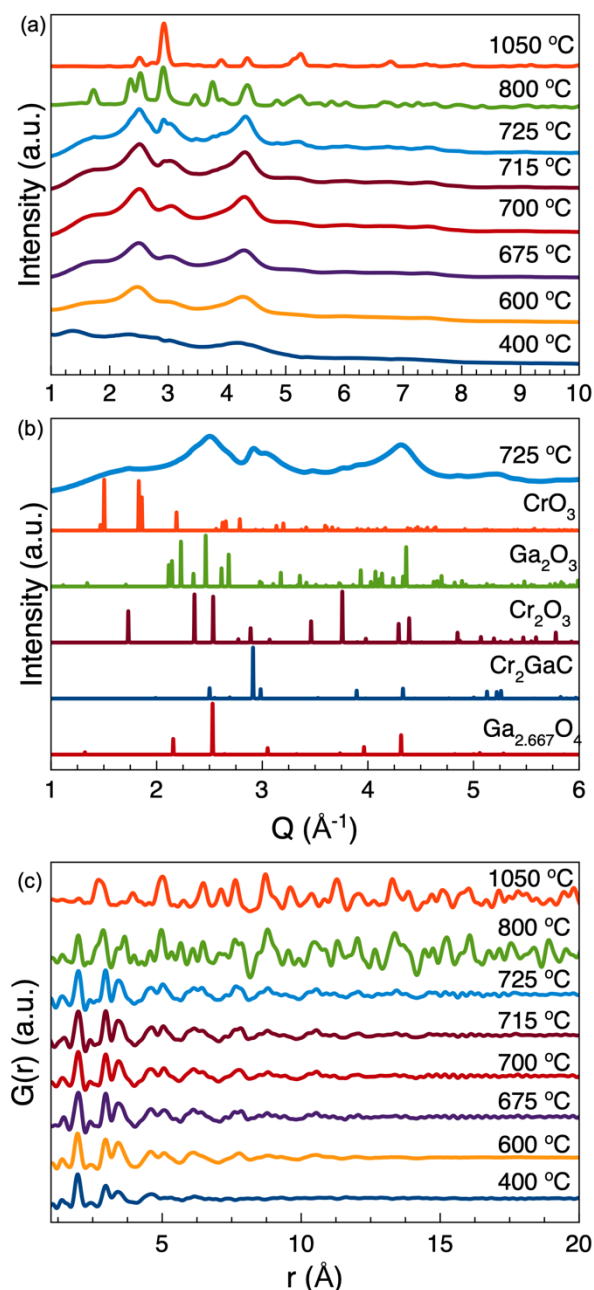

Figure 2: X-ray diffraction data obtained from the 8 samples collected at different stages of the reaction. **(b)** Comparison of the diffraction data obtained from the 725 °C sample to the diffraction patterns of selected chromium and gallium oxides. **(c)** The resulting PDFs from the diffraction data in (a).

Turning to the mechanistic part of this study, we start by looking at the scattering patterns obtained from 8 points throughout the reaction, which are shown in Figure 2 (a). The reaction was terminated at 400, 600, 700, 715, 725, 800, and 1050 °C and the products were subsequently structurally characterized. Based on the X-ray diffraction data the initially formed phases between 400 – 725 °C are barely crystalline and show only a few broad diffuse scattering features. Upon heating to 800 °C crystalline compounds are formed, mainly the MAX phase of interest, Cr_2GaC and Cr_2O_3. Upon further heating to 1050 °C Cr_2O_3 is consumed leaving the MAX phase as the only major component.

However, to understand the chemistry occurring during the synthesis we need to understand the structural chemistry occurring prior to the formation of the crystalline compounds. As shown in Figure 2 (b) it is not possible to index the few features present in the diffraction data at lower temperatures to any known crystal structure. Instead, we Fourier transform the X-ray scattering patterns into the X-ray PDFs to better analyze the atomic structure (Figure 2 (c)).

The PDF obtained from the samples synthesized between 400 °C and 725 °C are more or less identical except for the PDF range itself which increases with increasing temperature. This shows that no structural changes occur during the heating from 400 to 725 °C, but that the formed atomic structure only increases in ordering. The fits in Figure S 2 show that neither the Cr_2GaC structure nor the Cr_2O_3 structure can describe the atomic structure of the formed nanostructure.
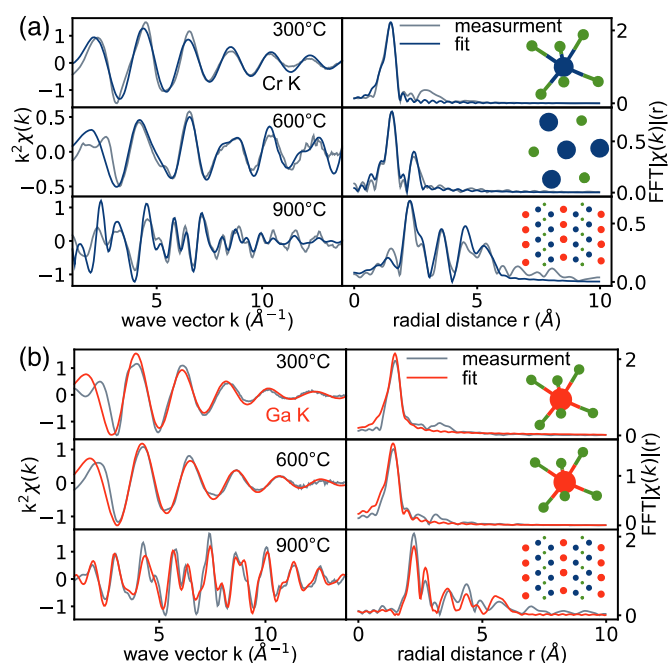

Figure 3: EXAFS data and fits of the **(a)** Cr K-edge and **(b)** Ga K-edge of the three prepared samples. Measurements are indicated in grey, corresponding fits are coloured. Fast Fourier transform is not phase corrected.

Instead, the initially formed atomic structure is different from crystal structures formed at higher temperatures. The first major peak in the X-ray PDF is at 1.8 Å which correspond to either a *M-O* (*M* = Ga or Cr) or a Cr-C distance since Ga does not form direct bonds with C. As exemplified in the calculated PDFs in Figure S 1, the Cr-C peak is very weak because the number of Cr-C distances in chromium carbides is very low. Instead, the intense X-ray PDF peak at 1.8 Å suggests the formation of an oxide, which is also supported by the EXAFS data presented (Figure 3). Similar to the total scattering studies, X-ray absorption spectroscopy data of the Cr and Ga K-edges were recorded. Here, the reaction was again terminated at different states to gain insight into the early (300 °C), mid (600 °C), and end stage (900 °C) of the reaction. Looking at the extended fine structure the local environment of the absorbing atom (Cr or Ga) is uncovered, as well as the electronic structure by analyzing the near edge (see SI, Figure S 4). Figure 3 presents the EXAFS measurements of both the Cr and Ga K-edge at different reaction temperatures including the according fits. Based on that, and in line with the PDF analysis, the data suggest that the neighboring atoms around Cr are either C or O (paths taken from the Cr_2O_3 structure). Because of the similarity of C and O, a clear distinction solely based on EXAFS is not feasible, however, taking the PDF results into consideration, C can confidently be ruled out. Looking at the scattering paths of the low- and mid-temperature state of the reaction, no significant change takes place, which was already observed in the PDF data (Figure 2 (c)). The notable change takes place after heating the reaction to completion (see Figure 3). However, the environment of the absorbing Cr atom changes when reaching 600 °C, which can be due to a starting crystallization or increase in long range ordering. This is indicated by the second peak in the FFT, which can be attributed to an additional Cr atom at roughly 2.9 Å. This observation is again in line with the PDF analysis, where an increased long-range ordering is observable in this temperature regime.

The X-ray PDF and the EXAFS data show that the first structure formed is an oxide. However, Cr and Ga are not commonly known to form any oxides containing just the two metals. With other transition metals, such as Mn, gallium tends to form oxides with the spinel structure.[29] Initially, it was attempted to describe the obtained PDF at 725 °C with a spinel structure where we placed Ga on all metal sites to simplify the model and the resulting fit is shown in Figure 4 (a). The dampening from the size of the nanostructure was refined through a spherical dampening envelope. The spinel does a fairly decent job describing the PDF. From the spinel fit it is possible to identify the interatomic distances giving rise the first three peaks of the X-ray. The first is, as already mentioned, the M-O peak as indicated in Figure 4 (b). The second peak at 3 Å is the M-M distance between two octahedrally coordinated metal ions, O_d. The third is the M-M distance between a tetrahedrally coordinated metal ion and an octahedrally coordinated metal ion, T_d. All three distances are also shown in Figure 4 (b). These three fundamental peaks are present already at 400 °C. Combining the spinel structure with other crystal structures such as Ga_2O_3 or Cr_2O_3 did not improve the fit.
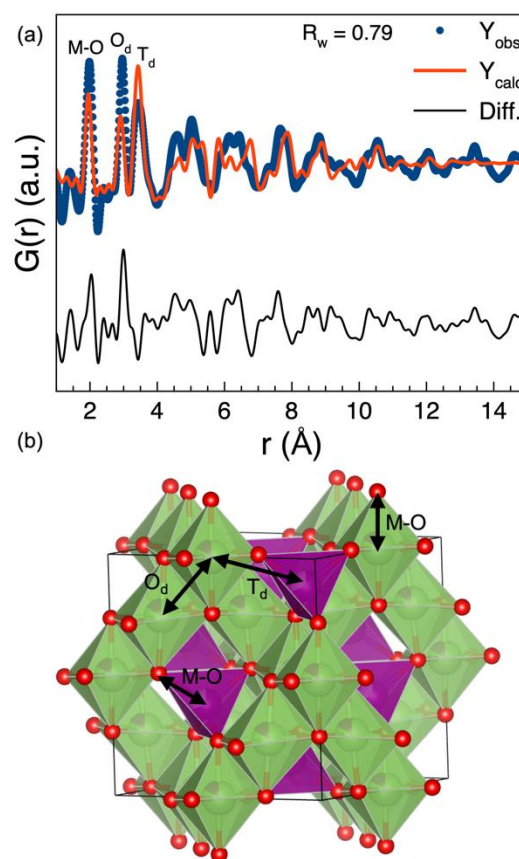

Figure 4: (a) Fit of a $MnGaO_4$ spinel crystal structure with Mn replaced with Ga to the PDF obtained from the 725 °C sample. The 3 indexed peaks correspond to the 3 distances shown in the reported spinel crystal structure shown in **(b)**. Mn is shown in purple, Ga in green and O in red, with the polyhedral reflecting this color scheme.

However, the spinel model has two main issues. Firstly, O_d is slightly too short and the peak corresponding to T_d is too intense. The intensity of a PDF peak is related to the number of distances contributing to the peak and the scattering length of the atoms involved. It would be tempting to explain the lower intensity of the T_d peak with the presence of Cr on the tetrahedral site because Cr is a weaker scatterer of X-rays than Ga. Unfortunately Cr(III) has a strong preference for octahedral coordination,[30] while Ga(III) in oxides can have both tetrahedral and octahedral coordination. Therefore, it is highly unlikely that Cr is placed on the tetrahedral site. Instead, it is observed in nanostructured spinel oxides where the overall occupancy of the tetrahedral site is lower than 1.[31,32] Refining the overall occupancy of the tetrahedral site gives the fit in Figure 5 (a), which solves the excess intensity of the T_d peak. Sadly, this does not solve the too short O_d distance as seen in the inset in Figure 5 (a).

This means that the spinel structure is not the correct description of the nanostructured oxide as shown in Figure 4 (a). However, since the spinel structure provided a reasonable description of the PDF, the nanostructured phase formed at lower temperatures should resemble a spinel oxide with octahedral and tetrahedral sites. Probably with a lower occupancy of the tetrahedral sites. As shown in Figure S 3 in the supporting information several Ga_2O_3 structures

with octahedrally and tetrahedrally coordinated metal ions provides a good description of the PDF. However, the PDF is decisively best described using a spinel-oxide-like $VO_{1.3}$ phase,[33] shown in Figure 5 (b). As shown in Figure 5 (c) $VO_{1.3}$ has 3 different octahedral and two different tetrahedral sites. The tetrahedral and octahedral site marked in Figure 5 (c) have their occupancy linked so that the total sum is equal to 1, suggesting that if one of the sites is occupied the other is not. Refining this ratio leads to the fit in Figure 5 (b) with a 0.28 occupancy on the tetrahedral site. The refined structure has an overall stoichiometry of $M_{52}O_{64}$ and with both metals being in oxidation state 3+ this is not a charge balanced formula.

The charges can be balanced if the metal sites have an average occupancy of 32/39 or around 0.82051. However, this does not change the fit, except for the tetrahedral occupancy which instead refines to 0.22. In general, trying to refine the occupancies further, e.g., the Cr and Ga ratio on the different sites does not change the fit, which means that the X-ray PDF data obtained here are not sensitive enough to detect the distribution of the Ga and Cr on the different metal sites. Instead, Ga was assumed on all metal sites. Several refinements with a second phase, e.g. Cr_2O_3 and Cr_2GaC were also attempted, but none of them indicated the presence of a second phase.

The unit cell refines to a = 11.52 Å and c = 8.62 Å, but the spherical diameter of the crystallite size refines to only 17 Å. Therefore, the largest nanostructure formed at 725 °C could not even contain 2 complete unit cells. At lower temperatures, where the atomic structure is the same, the ordering in the PDF is smaller than even a single unit cell. It does therefore not make sense to describe the nanostructured oxide formed initially in the sol-gel synthesis with a crystal structure. We want to emphasize that the $VO_{1.3}$ should not be considered as a unique model, which is evident from the fact that several similar oxides provide almost as good fits (Figure S 3). Instead, obtained is a description of the structural motifs in the atomic structure. In this case the gallium nitrate and chromium nitrate break down to form a nanostructured oxide with tetrahedrally and octahedrally coordinated metal ions which resembles the atomic structure observed in the crystal structures of spinel oxides and other related oxides such as $VO_{1.3}$. The sample synthesized at 400 °C is only ordering to 6 Å and it might be more correct to consider this structure as an amorphous structure with tetrahedrally and octahedrally coordinated metal ions.
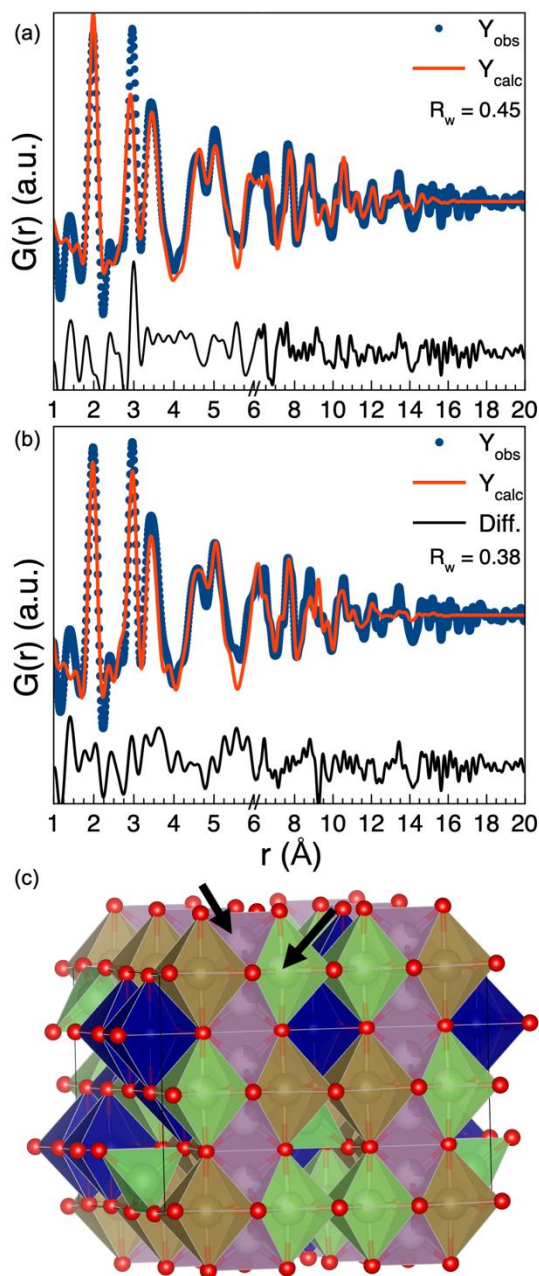

Figure 5: (a) Fit of the spinel structure in Figure 4b to the PDF obtained from the 725 °C sample with the occupancy of the tetrahedral site refined. The inset shows that the O_d distance of the spinel structure is too short to describe the experimental PDF. **(b)** Fit of the $VO_{1.3}$ phase to the PDF obtained from the 725 °C sample. **(c)** $VO_{1.3}$ crystal structure. The arrows indicate the two sites which occupancy ratio is refined in the fit in (b). O is shown in red, and the remaining atoms are Ga. The colors of the polyhedra correspond to different metal sites in the $VO_{1.3}$ structure.

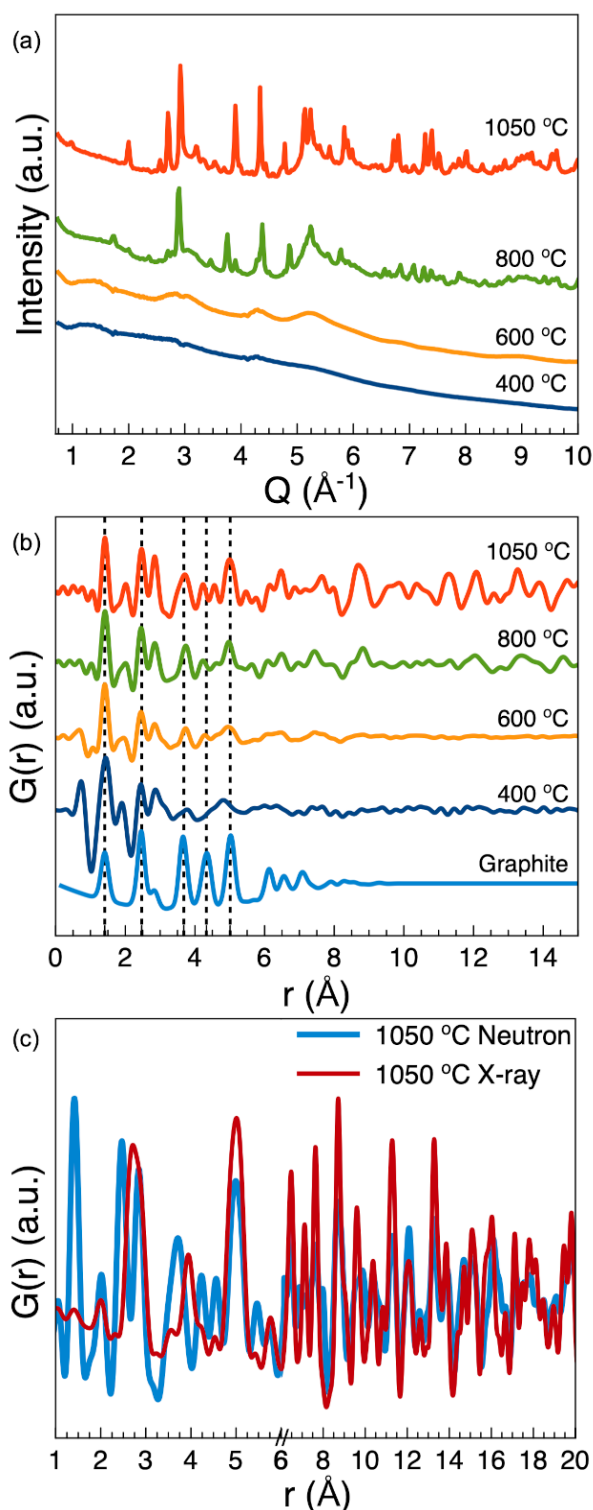**Figure 6: (a)** Neutron total scattering data obtained for the 400, 600, 800 and 1050 °C samples. **(b)** PDFs obtained from the scattering patterns in (a) compared to a calculated PDF of graphite with a crystallite size of 8 Å. **(c)** Comparison between the X-ray and neutron PDFs obtained from the 1050 °C sample.

The X-ray PDF reveal that upon heating the gel formed from water, metal nitrates and citric acid, it is transformed into a nanostructured oxide. Upon heating to 800 °C the nanostructured oxide is converted into much more crystalline oxides. The crystalline oxides are then reduced to form the MAX phase. This is further supported by the
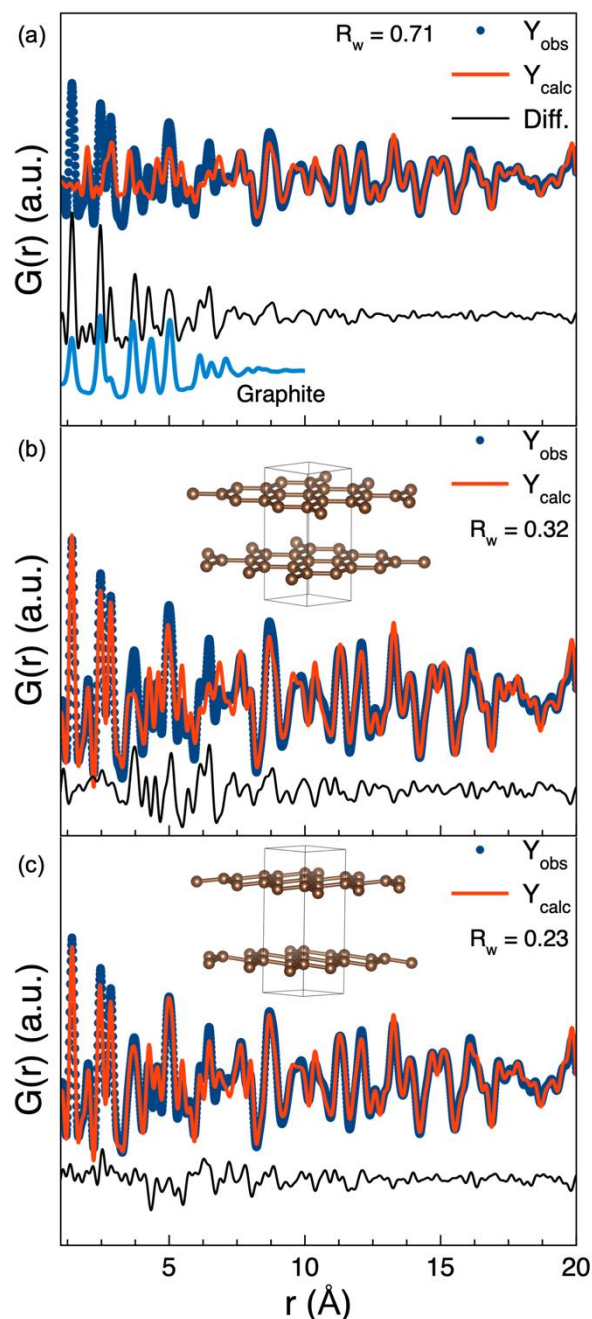

Figure 7: (a) Fit of the crystalline structures to the neutron PDF obtained from the 1050 °C sample. The difference curve is compared to a calculated PDF of graphite with an 8 Å crystallite size. **(b)** Fit using nanostructured graphite and the crystalline structures obtained from the Rietveld refinement to neutron PDF obtained from the 1050 °C sample. **(c)** Same fit as in (b), but where disorder has been introduced in the graphite model by refining the z position of the C atoms.

EXAFS data in Figure 3, where the high temperature data clearly show scattering paths for Cr_2GaC, as well as the near-edge analysis (Figure S 4), which indicates a change in oxidation state and a possible gradual exchange of O with C.

The carbon is not reacting with the Cr and Ga until the very end of the reaction and must therefore be bound somewhere until the temperatures are high enough to facilitate the reduction of the oxide (see also Figure 8). Citric acid decomposes at temperatures around

175 °C[34] (which is also observed in the DTA-MS data, see below Figure 8) and in order to better detect the carbon we turned to neutron total scattering and pair distribution function. The neutron total scattering and the resulting PDFs are shown in Figure 6 (a) and (b). The neutron PDF and the X-ray PDF from the 1050 °C sample are compared in Figure 6 (c) and the neutron PDF data contain several
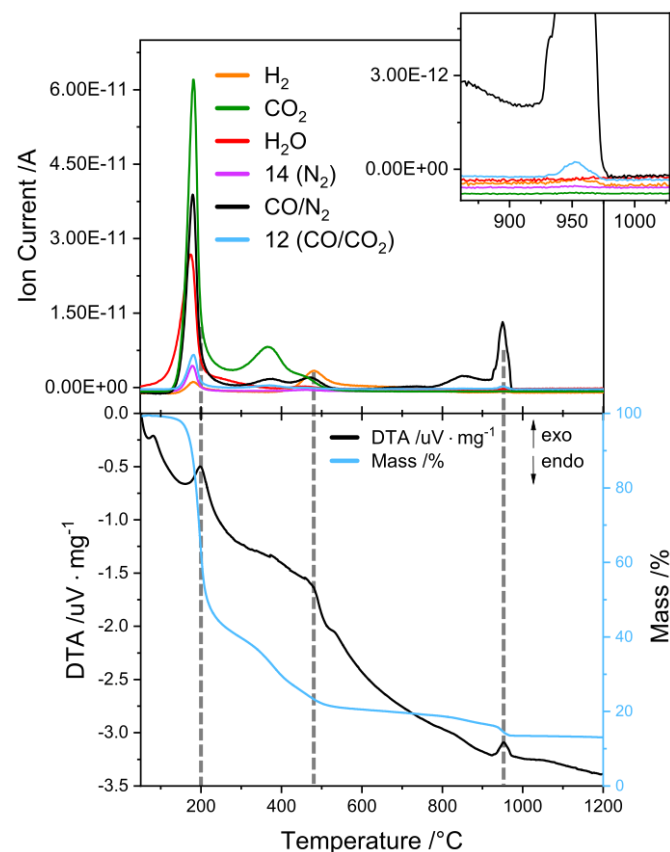

Figure 8: (Top) Semiquantitative MS data of the major gases emerging from the Cr_2GaC gel upon heating. Traces denoted with their respective m/z cannot be unambiguously assigned to a single gas. Here, possible gases are listed in parentheses. **(Bottom)** DTA-TG recorded simultaneously. Grey dashed lines added as a guide to the eye.

intense peaks that are not present in the X-ray PDF. Most noticeable are the three peaks at 1.4 Å, 2.45 Å and 3.75 Å.

We can isolate the contribution from the structure giving rise to these peaks by fitting the neutron PDF obtained from the 1050 °C sample with the crystalline models used in the Rietveld refinements (see Figure 1). This yields the fit shown in Figure 7 (a), which shows that the crystalline structure describes the neutron PDF very well beyond 8 Å. Below 8 Å a nanostructured phase makes a major contribution to the experimental neutron PDF. As shown in Figure 7 (a) the PDF peaks not described by the crystalline phases can be identified as the interatomic distances in graphite. Including a nanostructured graphite phase with a spherical crystallite of 8 Å in the fit of the neutron PDF yields the fit in Figure 7 (b). The graphite model greatly improves the fit of the first 8 Å, however as indicated in Figure 7 (b) there are still a few peaks which cannot be fitted by the model. It is well-known that the carbon sheets in disordered carbon are not completely ordered.[35–37] We can introduce the

disorder in the carbon sheets by breaking the space group symmetry of graphite and refine the z coordinate of the carbon atoms in the graphite model. This results in the fit and the structure in Figure 7 (c). The peaks from the nanostructured disordered graphite are present in the PDFs obtained from the 400, 600, 800, and 1050 °C samples which show that already at 400 °C the citric acid has decomposed to a nanostructured disordered graphite-like phase, which is in line with the DTA-MS data (see Figure 8 and following discussion) as well as expectation for this reaction based on the decomposition temperature of citric acid.[38] The PDF obtained from the 400 °C samples contain a major negative peak at roughly 1 Å. Only bonds involving hydrogen have a length of 1 Å and hydrogen is also the only element in the synthesis which has a negative neutron scattering length. The peak disappears when heating to 600 °C, which is again in line with the DTA-MS data that show the emission of hydrogen around 500 °C. PDF cannot reveal what the hydrogen is bonded to, but it is likely the carbon species.

The DTA-MS analysis (Figure 8), as previously mentioned, supports the mechanistic hypotheses. The reaction commences with the decomposition of the organics, accompanied by a major mass loss around 200 °C. Expectedly, these reactions release mainly CO_2, CO (decomposition under oxygen deficiency), and H_2O, but also some elemental nitrogen contributions are detectable (due to fragmentations visible both in the CO/N_2 trace and the m/z 14 trace, confirming the presence of nitrogen). The latter is in line with a previous study on sol-gel derived Cr_2GaC and stems from the utilized nitrate precursors.[4] The next major reaction is the formation of the oxidic species discussed earlier, accompanied by the release of hydrogen gas, as hypothesized based on the PDF analysis. The final reduction reaction mentioned earlier is also visible in the DTA-MS data. Around 950 °C, an exothermic peak alongside the final mass loss occurs during the last peak of CO leaving the system. Here, based on the absence of both CO_2 and m/z 14 (i.e., N_2), the CO/N_2 signal (m/z 28) can be unambiguously assigned to CO, which is further strengthened by the presence of m/z 12 (possible fragments of CO and CO_2, inset Figure 8). Interestingly, the reduction appears to occur at two temperatures, about 100 °C apart at 850 °C and 950 °C. It is reasonable to assume that the reduction commences around 800 °C and reaches its maximum above 900 °C, which is the temperature where the equilibrium between graphite and oxygen peaks in favor of the reducing agent CO (Boudouard equilibrium).[39] This is also reflected in the peak intensities, which reach the maximum at higher temperatures.

Based on this, the reduction via CO, and PDF analysis of the graphite species, we can provide some guidance around the applicability of the sol-gel method within the MAX phase family. Firstly, highly oxophilic metals, such as Al or Ti, will require very high temperatures to allow for the reduction,[40] at which point the MAX phase might not form due to the very high reaction temperature. Secondly, the reductive power reaches a maximum around 1000 °C,[39] which means the most efficient systems should have synthesis temperatures in that regime, which again requires the metals to be reducible at or

below that threshold. Moving forward, the Ellingham diagrams[40] give guidelines as to which metal combination in the MAX phase family is a potential viable pairing with sol-gel chemistry. It should be noted, however, that the Ellinghams diagrams are based on bulk solid-state data, and hence, might not accurately predict the behavior in sol-gel based reactions. In fact, based on a very recent work,[41] we found Cr_2GeC and V_2GeC to be viable candidates for this technique, proving two points: (i) compounds with a synthesis temperatures around the 1000 °C threshold are feasible if their composition excludes oxophilic metals; (ii) Ellingham diagrams need to be used cautiously as all metals in that study (Cr, V, Ge) have reported reduction temperatures that are (partly significantly) higher than the synthesis temperature used. Based on these three MAX phases, the discussed mechanism appears to be generally applicable, where the initial combustion of the carbon source leads to the formation of nanostructured, disordered graphite, and the initially formed metal-oxygen species are replaced by bulk oxides before the final reduction into the target phase occurs. Hence, the present study easily transcends into other realms of materials chemistry and can be used as a guide for materials syntheses both for more complex ternary carbides as well as binaries.
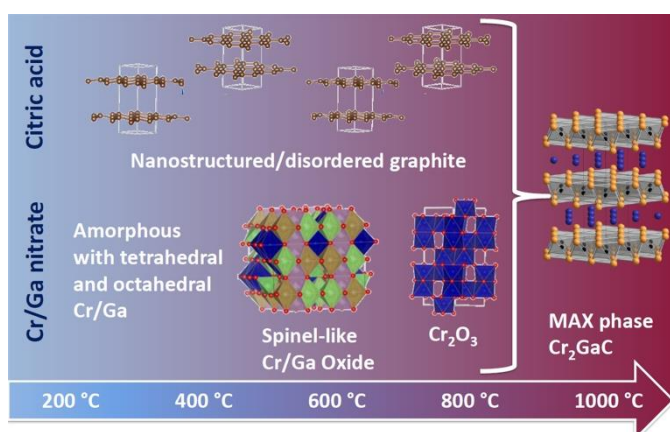

Figure 9: Schematic overview of the most critical steps in the sol-gel reaction forming Cr_2GaC, as elucidated based on the presented data.

Using both the neutron and X-ray PDF, EXAFS, and DTA-MS we have identified the important structural steps in the sol-gel synthesis of Cr_2GaC and the reaction can be summarized as done in Figure 9. First the citric acid is decomposed to a nanostructured disordered graphite-like structure, while simultaneously the metal nitrates are forming a nanostructured oxide with tetrahedrally and octahedrally coordinated metal ions. Upon heating the oxides grow and eventually form bulk oxides, primarily Cr_2O_3. Finally, the carbon reduces the oxides to form the desired MAX phase.

Conclusions

The present study successfully provides profound insights into the reaction mechanism of sol-gel synthesized MAX phase Cr_2GaC. We show, by employing a variety of advanced *ex-* and *in-situ* techniques, light can be shed onto reactions taking place even at comparably low temperatures where no crystalline phases have formed yet. Using

this approach, we conclude that the sol-gel synthesis of Cr_2GaC consists of two separate reactions taking place beside one another, and only at the very end merge into the final product-yielding reaction. While citric acid decomposes into nanostructured amorphous graphite, the metal nitrates undergo a multitude of changes along the way until the ultimately formed crystalline oxides are reduced by the graphite and Cr_2GaC is formed. Based on this knowledge, we provide guidelines and propose a certain extrapolability of this mechanism to other MAX phases and in general, carbides. Due to the initial oxidation of metals, we suggest to be limited to those metals that can be reduced by graphite around 1000 °C, as that temperature provides the strongest reductive atmosphere. Furthermore, as the graphite side of the mechanism is not directly linked to the metals initially, these findings explain the interchangeability of the carbon source demonstrated in various ways in the literature.

Author Contributions

Jan P. Siebert synthesized the samples, provided XRD, SEM, and DTA-MS analyses, and wrote the manuscript. Mikkel Juelsholt provided XRD, NPD, and PDF analyses, and wrote the manuscript. Damian Günzing contributed the EXAFS analysis and wrote the manuscript. Christina S. Birkel provided the research plan and wrote the manuscript.

Conflicts of interest

There are no conflicts to declare.

Acknowledgements

References

1. Ebelmen, E. von. *Justus Liebigs Annalen der Chemie*. **57**, (1846).

2. Walsh, D., Wimbush, S. C. & Hall, S. R. Reticulated superconducting YBCO materials of designed macromorphologies with enhanced structural stability through incorporation of lithium. *Supercond. Sci. Technol.* **22**, 015026 (2009).

3. Dollé, M. *et al.* Synthesis of nanosized zirconium carbide by a sol–gel route. *J. Eur. Ceram. Soc.* **27**, 2061–2067 (2007).

4. Siebert, J. P. *et al.* Sol–gel based synthesis and enhanced processability of MAX phase Cr_2GaC. *J. Mater. Chem. C* **7**, 6034–6040 (2019).

5. Giordano, C. & Antonietti, M. Synthesis of crystalline metal nitride and metal carbide nanostructures by sol–gel chemistry. *Nano Today* **6**, 366–380 (2011).

6. Venugopal, S. *et al.* Sol-gel synthesis and formation mechanism of ultrahigh temperature ceramic: HfB_2. *J. Am. Ceram. Soc.* **97**, 92–99 (2014).

7. Danks, A. E., Hall, S. R. & Schnepp, Z. The evolution of sol-gel chemistry as a technique for materials synthesis. *Mater. Horizons* **3**, 91–112 (2016).

8. Siebert, J. P., Flores, M. & Birkel, C. S. Shape Control of MAX Phases by Biopolymer Sol–Gel Synthesis: Cr_2GaC Thick Films, Microspheres, and Hollow Microspheres. *ACS Org. & Inorg. Au* (2021).

9. Siebert, J. P., Hajra, D., Tongay, S. & Birkel, C. S. The synthesis and electrical transport properties of Carbon/Cr_2GaC MAX phase composite microwires. *Nanoscale* (2021). doi:10.1039/D1NR06780J

10. Cheetham, A. K. & Mellot, C. F. In Situ Studies of the Sol-Gel Synthesis of Materials. *Chem. Mater.* **9**, 2269–2279 (1997).

11. Wilkinson, A. P., Speck, J. S., Cheetham, A. K., Natarajan, S. & Thomas, J. M. In situ x-ray diffraction study of crystallization kinetics in $PbZr_{1-x}Ti_xO_3$, (PZT, x = 0.0, 0.55, 1.0). *Chem. Mater.* **6**, 750–754 (1994).

12. Schnepp, Z. *et al.* In Situ Synchrotron X-ray Diffraction Study of the Sol–Gel Synthesis of Fe_3N and Fe_3C. *Chem. Mater.* **27**, 5094–5099 (2015).

13. Schnepp, Z. A. C., Wimbush, S. C., Mann, S. & Hall, S. R. Structural Evolution of Superconductor Nanowires in Biopolymer Gels. *Adv. Mater.* **20**, 1782–1786 (2008).

14. Charpentier, P. A., Li, X. & Sui, R. Study of the Sol–Gel Reaction Mechanism in Supercritical CO_2 for the Formation of SiO_2 Nanocomposites. *Langmuir* **25**, 3748–3754 (2009).

15. Rohde, H. & Kudielka, H. Strukturuntersuchungen an Carbosulfiden von Titan und Zirkon. *Zeitschrift für Krist. - Cryst. Mater.* **114**, 447–456 (1960).

16. Jeitschko, W., Nowotny, H. & Benesovsky, F. Kohlenstoffhaltige ternäre Verbindungen (H-Phase). *Monatshefte für Chemie* **94**, 672–676 (1963).

17. Barsoum, M. W. & El-Raghy, T. Synthesis and Characterization of a Remarkable Ceramic: Ti_3SiC_2. *J. Am. Ceram. Soc.* **79**, 1953–1956 (1996).

18. Radovic, M. & Barsoum, M. W. MAX phases: bridging the gap between metals and ceramics. *Am. Ceram. Soc. Bull.* **92**, 20–27 (2013).

19. Siebert, J. P. *et al.* Structure determination and magnetic properties of the Mn-doped MAX phase Cr_2GaC. *Mater. Chem. Front.* (2021).

20. Juhás, P., Davis, T., Farrow, C. L. & Billinge, S. J. L. PDFgetX3 : a rapid and highly automatable program for processing powder diffraction data into total scattering pair distribution functions. *J. Appl. Crystallogr.* **46**, 560–566 (2013).

21. Yang, X., Juhas, P., Farrow, C. L. & Billinge, S. J. L. xPDFsuite: an end-to-end software solution for high throughput pair distribution function transformation, visualization and analysis. (2014).

22. Neuefeind, J. C. Nanoscale-Ordered Materials Diffractometer NOMAD.

23. McDonnel, M. T. *et al.* ADDIE: ADvanced DIffraction Environment – A Software Environment for Analyzing Neutron Diffraction Data. *Acta Crystallogr. Sect. A* **73**, (2017).

24. Juhás, P., Louwen, J. N., van Eijck, L., Vogt, E. T. C. & Billinge, S. J. L. PDFgetN3: Atomic pair distribution functions from neutron powder diffraction data using ad hoc corrections. *J. Appl. Crystallogr.* **51**, 1492–1497 (2018).

25. Farrow, C. L. *et al.* PDFfit2 and PDFgui: computer programs for studying nanostructure in crystals. *J. Phys. Condens. Matter* **19**, 335219 (2007).

26. Rehr, J. J., Kas, J. J., Vila, F. D., Prange, M. P. & Jorissen, K. Parameter-free calculations of X-ray spectra with FEFF9. *Phys. Chem. Chem. Phys.* **12**, 5503 (2010).

27. Newville, M. Larch: An Analysis Package for XAFS and Related Spectroscopies. *J. Phys. Conf. Ser.* **430**, 012007 (2013).

28. Jeitschko, W., Nowotny, H. & Benesovsky, F. Kohlenstoffhaltige ternäre Verbindungen (V-Ge-C, Nb-Ga-C, Ta-Ga-C, Ta-Ge-C, Cr-Ga-C und Cr-Ge-C). *Monatshefte für Chemie* **94**, 844–850 (1963).

29. Casado, P. G. & Rasines, I. Crystal data for the spinels MGa_2O_4 (M= Mg, Mn). *Zeitschrift für Krist. - Cryst. Mater.* **160**, 33–38 (1982).

30. Vincent, J. B. Chromium: Properties and Determination. in *Encyclopedia of Food and Health* 114–118 (Elsevier, 2016). doi:10.1016/B978-0-12-384947-2.00161-6

31. Jensen, K. M. Ø. *et al.* Mechanisms for Iron Oxide Formation under Hydrothermal Conditions: An in Situ Total Scattering Study. *ACS Nano* **8**, 10704–10714 (2014).

32. Cooper, S. R. *et al.* Evolution of Atomic-Level Structure in Sub-10 Nanometer Iron Oxide Nanocrystals: Influence on Cation Occupancy and Growth Rates. *ACS Nano* **14**, 5480–5490 (2020).

33. Gusev, A. I., Davydov, D. A. & Valeeva, A. A. Vacancy distribution in nonstoichiometric vanadium monoxide. *J. Alloys Compd.* **509**, 1364–1372 (2011).

34. Barbooti, M. M. & Al-Sammerrai, D. A. Thermal decomposition of citric acid. *Thermochim. Acta* **98**, 119–126 (1986).

35. Franklin, R. E. The interpretation of diffuse X-ray diagrams of carbon. *Acta Crystallogr.* **3**, 107–121 (1950).

36. Franklin, R. E. The structure of graphitic carbons. *Acta*

Crystallogr. **4**, 253–261 (1951).

37.   Harris, P. J. F. & Tsang, S. C. High-resolution electron microscopy studies of non-graphitizing carbons. *Philos. Mag. A* **76**, 667–677 (1997).

38.   Wyrzykowski, D., Hebanowska, E., Nowak-Wiczk, G., Makowski, M. & Chmurzyński, L. Thermal behaviour of citric acid and isomeric aconitic acids. *J. Therm. Anal. Calorim.* **104**, 731–735 (2011).

39.   Lide, D. R. *Handbook of chemistry and physics*. (CRC Press Boca Raton, Florida, 2004).

40.   Howard, S. M. Ellingham Diagrams. *J. Soc. Chem. Ind.(London)* **63**, 125 (1944).

41.   Siebert, J. P., Patarakun, K. & Birkel, C. S. Mechanistic Insights into the Nonconventional Sol–Gel Synthesis of MAX Phase M_2GeC (M = V, Cr). *Inorg. Chem.* **61**, 1603–1610 (2022).

42.   Giordano, C., Erpen, C., Yao, W., Milke, B. & Antonietti, M. Metal nitride and metal carbide nanoparticles by a soft urea pathway. *Chem. Mater.* **21**, 5136–5144 (2009).

43.   McMurdie, H. F., Morris, M. C., Evans, E. H. & Paretzkin, B. Standard X-ray diffraction powder patterns from the JCPDS research associateship. *Powder Diffr.* **2**, 45 (1987).